



Anchoring Ag_3PO_4 nanoparticles on MIL-101(Fe)@nanocellulose composite for tetracycline degradation

Nguyen Thi Hoa, Le Thi Nguyen, Vu Van Tai, Pham Xuan Nui*

Department of Chemical Engineering, Hanoi University of Mining and Geology

18-Vien Street, Duc Thang Distreet, Bac Tu Liem, Hanoi, Vietnam

**Email: phamxuannui@humg.edu.vn*

ARTICLE INFO

Received: 24/9/2021

Accepted: 17/10/2021

Published: 25/10/2021

Keywords:

Photocatalyst, Nanocellulose (NC)

Ag_3PO_4 @MIL-101(Fe)@NC,

Tetracycline (TC)

ABSTRACT

In this research, the combination of the photocatalytic activity of the semiconductor Ag_3PO_4 and the as-synthesized MIL-101(Fe)@nanocellulose (NC) from agricultural and bottle waste sources exhibited great photocatalytic efficiency. The Ag_3PO_4 @MIL-101(Fe)@nanocellulose (NC) composite has overcome the disadvantages of pure Ag_3PO_4 and significantly improved the photocatalytic activity. Structural characteristics, morphology of the materials were analyzed by X-ray diffraction (XRD), scanning electron microscopy (SEM), energy dispersive X-ray spectroscopy (EDX), and UV-vis diffuse reflectance spectroscopy (UV-vis DRS) methods. From the obtained results, composite has a narrow bandgap energy (2.45 eV) and excellent catalytic performance in the photodegradation of Tetracycline pollutants (99.7 % after 120 min). It demonstrates the development of new catalysts made from agricultural waste sources that show high stability, ease of fabrication and can operate in natural light for environmental remediation.

Introduction

Pharmaceuticals and cosmetics are known to be an emerging group of pollutants and receive the attention of scientists [1,2]. Several kinds of drugs such as antibiotics, hormones, preservatives are identified as existing in wastewater and drinking water. Among them, antibiotics receive special attention because they are widely used for both humans and veterinary medicine [3]. Tetracycline (TC) is one of the most frequently used antibiotics to therapeutics and growth promoters of cattle, pigs, poultry and fishery [4,5]. TC is used as a veterinary antibiotic that can enter the aquatic environment after animal manure is used as fertilizer, leading to potential impacts on aquatic and terrestrial organisms [6].

TC can easily decompose in a water solution by photocatalytic reactions in a short time [7]. Photocatalyst materials or semiconductors commonly used for the decomposition of TC are ZnO , TiO_2 [8,9]. Recently, silver phosphate (Ag_3PO_4) has attracted considerable attention because it has a narrow bandgap energy (about 2.4 eV) that can take advantage of 43% of the solar spectrum [10]. Therefore, Ag_3PO_4 is a promising candidate in the field of photocatalytic for the decomposition of organic pollutant compounds [11-13]. Several methods have been studied to increase the stability and catalytic properties of Ag_3PO_4 such as anion/cation doping, composite construction, metal deposition, and immobilization with support materials [12, 14-16].

The formation of the composite by coupling Ag_3PO_4 with support materials is a widely used method to enhance the visible-light response, improve the separation of electron-hole pairs, prevent their recombination, and enhance stability. Recently, organic metal frames (MOFs), consisting of metal ions clusters and organic ligands, are known as porous polymers with hollow structures, large surfaces and structural flexibility [17]. These favorable properties of MOFs allow them to become desirable hosts for immobilization or stabilization of nanoscales such as metal nanoparticles (NP), quantum dots (QDs), etc [18]. As such, MOFs represent great potential applications in gas adsorption and storage, sensors, heterogeneous catalysis, etc [19]. Among those MOFs, MIL-101(Fe) is a kind of metal-organic framework with excellent thermal stability, high specific area, excellent adsorption performance, and a friendly environment [20].

In addition, hybrid bio-inorganic nanostructures are promising materials for energy and environmental applications and biodegradable towards a circular economy [21]. Nanocellulose (NC) is a potential functional material due to they have natural origin, abundant raw resources, reproducibility, and flexible surface chemistry. They are applied for adsorption, energy conversion, electronics, gas sensors and catalysis [22,23]. Manali *et al.* [24] has studied the development of nanocellulose- TiO_2 composite material to remove volatile organic compounds and arsenic in wastewater through photocatalytic decomposition. Nanocellulose is seen as an insulating substrate that can mechanically support to NP, minimize the aggregation of nanoparticles, and the functional group available to cellulose can interact with the pollutant [25,26].

In this study, a combination of MIL-101(Fe) and nanocellulose could create a promising supporting material. The central metal atoms in MIL-101(Fe) can form coordinated bonding with carboxyl groups in cellulose, which can facilitate the immobilization and distribution of Ag_3PO_4 nanoparticles on the surface MIL-101(Fe)@NC composites, thus improving stability and increasing the ability to decompose pollutants. The as-prepared Ag_3PO_4 @MIL-101(Fe)@NC composite was characterized by the different spectrometers, such as XRD, FT-IR, SEM, TEM, EDX mapping, XPS, UV-Vis DRS. The photocatalytic activity of the composite was also studied.

Experimental

Materials

Ethylene glycol (EG, >99%), sodium hydroxide (NaOH, >98%), sulfuric acid (H_2SO_4 , >98%), iron(III) chloride hexahydrate ($\text{FeCl}_3 \cdot 6\text{H}_2\text{O}$, >99%), methanol (CH_3OH , >99.5%), dimethylformamide (DMF, >99.8%), hydrochloric acid (HCl, 37%) were purchased from Sinopharm Chemical Reagent Co. Ltd., China. Silver nitrate (AgNO_3 , >99.8%) was supplied by Sigma-Aldrich. Terephthalic acid was prepared following the procedure as previously reported [27]. Sugarcane bagasse collected from plantations located in Thanh hoa Province, Vietnam.

Synthesis of Ag_3PO_4 @MIL-101(Fe)@Nanocellulose

Synthesis of Nanocellulose

Extraction of cellulose from sugarcane bagasse

Sugarcane bagasse is washed and cut into 1-2 cm pieces. Process of treating impurities: sugarcane bagasse is submerged in a mixture of H_2O : Ethanol (1:1 v/v), stirred for 2 h at 60 °C, then washed with deionized water. The process of removing lignin: sugarcane bagasse after removing impurities was treated with 1 M NaOH solution at 80 °C for 2 h. The product was washed with distilled water until the neutral pH was reached. The process of removing hemicellulose: The product after that was treated with a mixture of 1% NaOH: 1% NaClO (1:1 w/v) solution at 80 °C for 1.5 h. After the reaction finish, the product was filtered, washed with distilled water and dried at 60 °C for 24h. Finally, the extracted cellulose has a white powder.

The synthesis of nanocellulose

The extracted cellulose from sugarcane bagasse was hydrolyzed by sulfuric acid (6.5M) solution with a ratio of cellulose and sulfuric acid 1:25 w/v. Then, the mixture solution was stirred for 45 min at 60 °C. After stirring, a colloidal was centrifuged at 6500 rpm for 30 min. Subsequently, the produced was washed with deionized until the neutral pH was reached. Finally, the product was stored in the refrigerator.

Synthesis of MIL-101(Fe)

The MIL-101(Fe) was synthesized using the solvothermal method. In this study, 1.082 g of $\text{FeCl}_3 \cdot 6\text{H}_2\text{O}$, 0.664 g of terephthalic acid, and 1 mL of acetic

acid were dissolved in 80 mL DMF and stirred continuously for 3 h at room temperature. The mixture was then transferred into a 100 mL Teflon-lined autoclave and heated up at 100 °C for 20 h. After natural cooling, the brown solid was extracted, refluxed with hot DMF and methanol three times. Then, the product was dried at 60 °C overnight. The product has the form of a light yellow powder.

One-pot synthesis of MIL-101(Fe)@NC

Firstly, 1.069 g of nanocellulose, 1.082 g FeCl₃.6H₂O, 0.664 g of terephthalic acid and 1 mL of acetic acid were dissolved in 80 mL N, N- dimethylformamide (DMF) and stirred continuously for 3 hours at room temperature. Then, the mixture was transferred into a 100 mL of Teflon-lined autoclave at 100 °C for 20 h. After natural cooling, the yellow solid was extracted, refluxed with hot DMF and methanol three times. Then, the product was dried at 60 °C overnight. The product has the form of a light yellow powder.

Preparation of Ag₃PO₄@MIL-101(Fe)@NC composite

Firstly, 0.5 g of MIL-101(Fe)@NC was dispersed in 50 mL of distilled water and stirred for 30 min. Subsequently, 0.342 g of Na₂HPO₄.12H₂O was dissolved in 30 mL of distilled water, then added into the above solution and the suspension was stirred for 30 min. After that, a particular amount of AgNO₃ solution (0.182 g, 0.243 g, 0.304 g with percentages of Ag₃PO₄ were 30, 40, and 50 wt.%, respectively) was added into the stirred above suspension dropwise. After reacting for 4 h, the product was collected via centrifugation, washed with distilled water several times, and dried at 60 °C for 24 h. The obtained composites were labeled as 30%, 40%, and 50% Ag₃PO₄@MIL-101(Fe)@NC.

Characterization

The crystal lattice structure of the synthesized samples was determined by X-ray powder diffraction (XRD) using a D8 ADVANCE system (Cu Kα₁ copper radiation, λ = 0.154 nm, 3° min⁻¹ scanning speed, Bruker,

Germany). Surface morphology was observed by a scanning electron microscope (S-4800, Hitachi). The Fourier transform infrared spectra (FT-IR) were measured with an FTIR Affinity-1S (SHIMADZU). X-ray energy dispersion (EDX) and EDX mapping were performed with a JED-2300 with a gold coating. The UV-vis diffuse reflectance (Uv-vis DRS) and were recorded with the UV-2600 spectrophotometer (Shimadzu). X-ray photoelectron spectroscopy (XPS) was conducted using an ESCALab 250 spectrometer (Thermo VG, UK).

Catalytic activity test

The photocatalytic activity was evaluated through the degradation reaction of tetracycline with a 125 W Xe lamp irradiation at room temperature. Specifically, 50 mg of the photocatalyst was dispersed in 30 mL of an aqueous solution containing TC (30 mL, 70 ppm). Prior to irradiation, samples were placed in the dark for 30 min to achieve the adsorption-desorption equilibrium, initial concentration (C₀) was taken at this point. Then, the mixture was illuminated under visible light for 120 min. After every 30 min, 3 mL suspension was taken out and filtered to remove the catalysts. The concentration (C_t) was analyzed using a UV-Vis 2450 spectrometer at maximum wavelength λ=357 nm. Tetracycline photodegradation performance was calculated by the following equation:

$$\% \text{ Degradation} = \frac{C_0 - C_t}{C_0} \times 100 \quad (1)$$

Where: C₀ is the initial concentration (t=0)

C_t is the concentrations at the time t ≠ 0

Results and Discussion

The crystal structure and phase composition of the samples were characterized by X-ray diffraction and Fourier-transform infrared (FT-IR) spectroscopy. The results are shown in Figure 1.

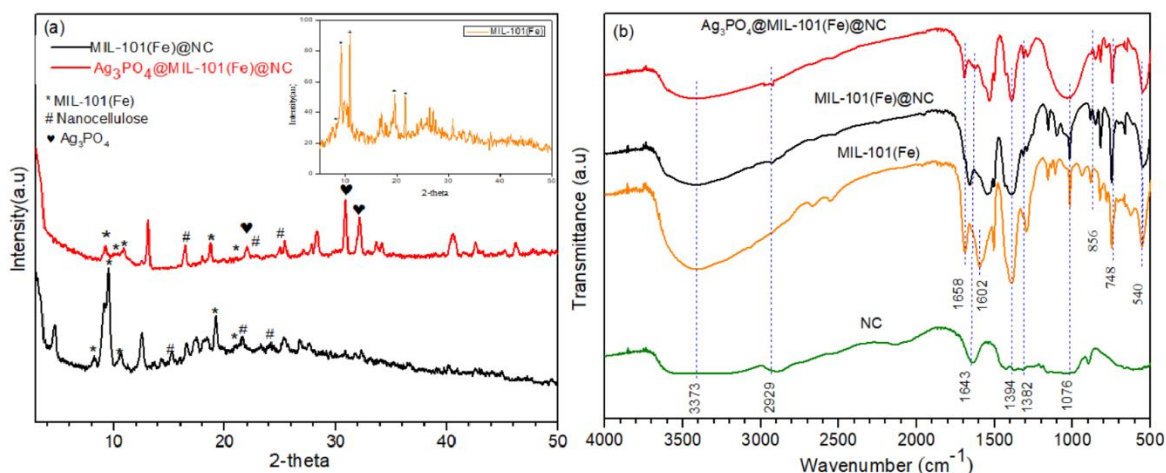


Figure 1: (a) XRD patterns of samples (a) MIL-101(Fe); (b) MIL-101(Fe)@NC, Ag₃PO₄@MIL-101(Fe)@NC. (b) FT-IR of nanocellulose, MIL-101(Fe), MIL-101(Fe)@NC, Ag₃PO₄@MIL-101(Fe)@NC

As shown in Figure 1, the main typical peaks of MIL-101(Fe) appeared at $2\theta = 8.4^\circ, 9.2^\circ, 10.7^\circ, 19.5^\circ, 21.5^\circ$. These sharp peaks with high intensity indicated that the obtained MIL-101(Fe) exhibited high crystallinity. As for MIL-101(Fe)@NC (Fig.1a), all the characteristic peaks of MIL-101(Fe) were maintained after decoration on nanocellulose. For nanocellulose, the main characteristic peaks at $2\theta = 15^\circ, 22.5^\circ, 34^\circ$ corresponding with (101), (040), (002) planes, can be attributed to the crystalline cellulose hydrolysis with acids that might remove the amorphous portion of cellulose [28]. Subsequently, the appearance of MIL-101(Fe) characteristic peaks demonstrated that the decoration of MIL-101(Fe) on NC did not change the natural characteristics of both materials. For the diffraction patterns of Ag₃PO₄@MIL-101(Fe)@NC, the diffraction peaks of Ag₃PO₄ were observed at $2\theta = 21.3^\circ, 33.6^\circ$ and 36.9° corresponded to the (110), (210), (211) crystal planes of cubic Ag₃PO₄, respectively, (JCPDS No. 06-0505) [29]. In addition, it is evident that those of the characteristic peaks of MIL-101(Fe) (*) and NC (#) didn't change, confirming that Ag₃PO₄@MIL-101(Fe)@NC composite has been successfully synthesized. The average crystalline size of composite powders was determined using Debye-Scherrer's equation:

$$D = \frac{k\lambda}{\beta \cos\theta} \quad (2)$$

Where D is the crystalline size, k is a shape factor, which is typically 0.9, λ is the Cu K α radiation wavelength ($\lambda = 0.154 \text{ nm}$), β is the line broadening at half the maximum intensity, and θ is the diffraction angle. The crystalline size was calculated for the diffraction angle $2\theta = 9.2^\circ$ of MIL-101(Fe) and the average crystalline of MIL-101(Fe), MIL-101(Fe)@NC,

and Ag₃PO₄@MIL-101(Fe)@NC was 23 nm, 28.4 nm and 32.9 nm.

Infrared spectroscopy was performed to determine the bond formation of materials. Figure 1 b shows the FT-IR spectrum of nanocellulose material, MIL-101(Fe), MIL-101(Fe)@NC, Ag₃PO₄@MIL-101(Fe)@NC composites. For nanocellulose, the absorption peaks at around 3300-3450 cm⁻¹ and 2890-2900 cm⁻¹ were attributed to the hydroxyl group O-H and aliphatic saturated C-H stretching vibrations, respectively [30,31]. The absorption peak at 1643 cm⁻¹ was indicated as the O-H vibration of absorbed water [32], even though the treated fibers were subjected to the drying process, the water adsorbed in the cellulose molecules is very difficult to be extracted due to the interaction between nanocellulose to water. The peak of C-H and C-O vibrations contained in the polysaccharide rings of cellulose is around 1382 cm⁻¹. The vibration of C-O-C in the pyranose ring was indicated by the absorption peak at 1051 cm⁻¹ [30]. The band at 892 cm⁻¹ represents C-O-C stretching vibrations. As for the MIL-101(Fe), the peaks at 552 cm⁻¹, 748 cm⁻¹ can be attributed to the Fe-O vibration, and the band at 1394 cm⁻¹ was from the aromatic carbon C-C vibrational mode, respectively [33]. The band at 1602 cm⁻¹ was attributed to C=O bonding in the carboxylate group [34]. As for the MIL-101(Fe)@NC composite, the characteristic peaks at 2900 cm⁻¹, 1643 cm⁻¹, 1602 cm⁻¹, 1394 cm⁻¹, 1368 cm⁻¹, 1051 cm⁻¹, 748 cm⁻¹, 552 cm⁻¹ were consistent with those of nanocellulose and MIL-101(Fe). Furthermore, for the Ag₃PO₄@MIL-101(Fe)@NC composite, all characteristic peaks of MIL-101(Fe)@NC are present and the typical O=P-O flexural vibrations and P-O asymmetric stretching vibration of PO₄³⁻ can be observed at 540 cm⁻¹ and 1076 cm⁻¹ [35]. The above

results further confirmed that the $\text{Ag}_3\text{PO}_4@\text{MIL-101}(\text{Fe})@\text{NC}$ has been successfully synthesized.

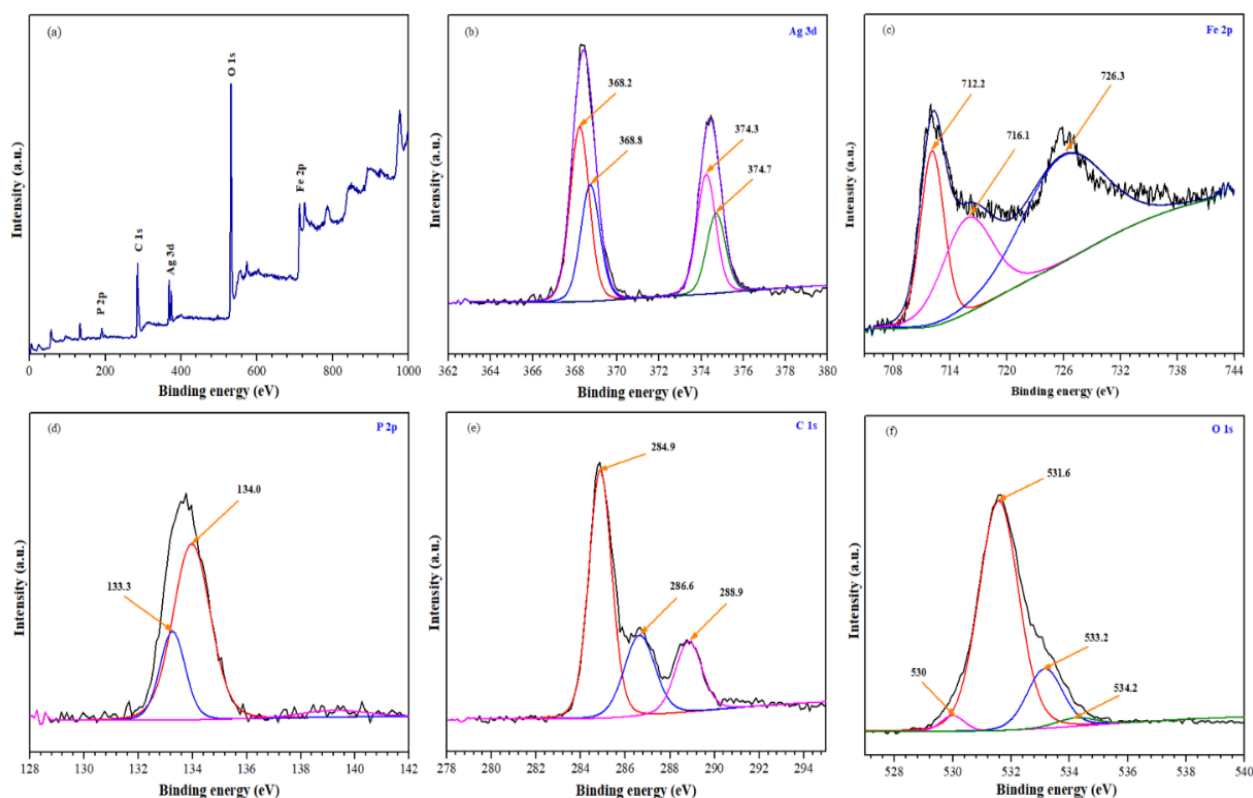


Figure 2 : (a) XPS survey spectrum of $\text{Ag}_3\text{PO}_4@\text{MIL-101}(\text{Fe})@\text{NC}$, high-resolution XPS spectra of (b) Ag 3d, (c) Fe 2p, (d) P 2p, (e) C 1s, and (f) O 1s

The chemical composition and binding energy of $\text{Ag}_3\text{PO}_4@\text{MIL-101}(\text{Fe})@\text{NC}$ were measured by XPS. The survey spectrum in Fig.2a indicated the presence of phosphorus, carbon, silver, iron, and oxygen. As shown in Fig.2b, two distinct peaks at 368.8 eV (Ag 3d_{5/2}) and 374.7 eV (Ag 3d_{3/2}) could be ascribed to the Ag in the composites. Further, the Ag 3d_{5/2} peak could be divided into two peaks at 368.2 and 368.8 eV, while the Ag 3d_{3/2} peak could be divided into peaks at 374.3 and 374.7 eV, respectively.

As shown, the peaks of 368.2 and 374.3 eV could be assigned to Ag, while the peaks of 368.8 and 374.7 eV could be attributed to metallic AgO, which is corresponding to previous literature [36]. In Fig.2c, the characteristic binding energy at 726.3 and 712.2 eV are assigned to the Fe 2p_{1/2} and Fe 2p_{3/2}, respectively [37]. The distance between these two peaks is about 14.2 eV, which agrees well with the typical features of Fe₂O₃ [38]. Moreover, the peak at 716.1 eV ascribed to the shakeup satellite of Fe(III) also deconvoluted. The above results further confirm the successful synthesis of MIL-101(Fe). Fig.2d, shows that the XPS peak of P

2p_{1/2}, P 2p_{3/2}, corresponding to P⁵⁺ in the PO₄³⁻ structure at the energies of 133.3 eV and 1334 eV. As shown in Fig.2e, the main binding energy of C 1s was presented by three peaks at 284.9, 286.6, 288.9 eV corresponding to C-C, C=C, O-C=O of phenyl and carboxyl group signals, respectively [39]. The O 1s spectrum consists of four peaks (Fig.2f), which could be assigned to O in O-C=O (534.2 eV), P-O-H (533.2 eV), Fe-O-Fe (530 eV) and P=O (531.6 eV), respectively [40].

Figure 3 shows the SEM and TEM images of nanocellulose, MIL-101(Fe), MIL-101(Fe)@NC, and $\text{Ag}_3\text{PO}_4@\text{MIL-101}(\text{Fe})@\text{NC}$ composite. As can be seen in Figure 3 (a,e), most of the individualized cellulose nanofibers were dispersed in water, and the cellulose nanofibers obtained were mainly 10–40 nm in width and a few microns in length. Figure 3. (b,f) shows the SEM and TEM images of synthesized MIL-101(Fe) particles, which have a special octahedral structure. This structure resembled the structure previously reported [41]. As shown in Figure 3. (c,g), the MIL-101(Fe) surface was covered by nanocellulose fibers.

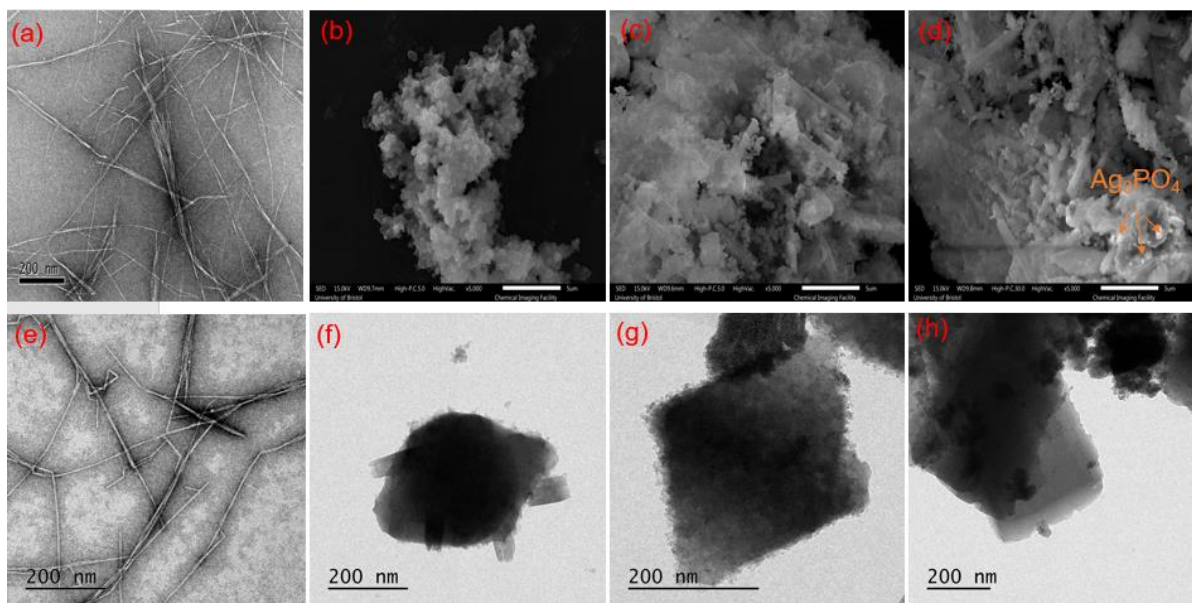


Figure 3: SEM images of (a) nanocellulose, (b) MIL-101(Fe), (c) MIL-101(Fe)@NC composite, (d) Ag₃PO₄@MIL-101(Fe)@NC composite; TEM of (e) nanocellulose, (f) MIL-101(Fe), (g) MIL-101(Fe)@NC composite, (h) Ag₃PO₄@MIL-101(Fe)@NC composite

Figure 4. (d,h) shows that the Ag₃PO₄ nanoparticles were distributed on the MIL-101(Fe)@NC composite, which has good dispersion with the morphology of the crystals was regular.

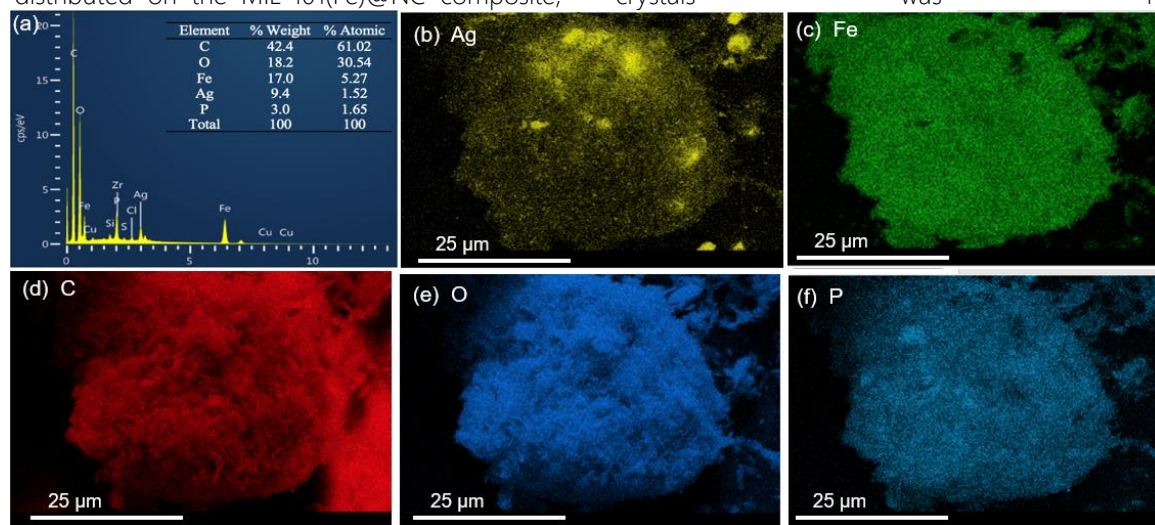


Figure 4 : (a) EDX spectrum and SEM micrograph with elemental mapping of (b) silver, (c) iron, (d) carbon, (e) oxygen, and (f) photpho of Ag₃PO₄@MIL-101(Fe)@NC composite

The elemental composition of the Ag₃PO₄@MIL-101(Fe)@NC sample was also confirmed by EDX spectrum and EDX mapping analysis. The EDX spectrum, as shown in Fig.4a demonstrated that the composite is composed of Ag, Fe, C, O, and P elements and also suggests the successful synthesis of composite material. From the results of the elemental mapping (Fig.4b-f), Ag and P elements were uniformly

distributed on the surface MIL-101(Fe)@NC and the results are in agreement with TEM images also.

Optical properties have a significant impact on the photocatalytic activity of the catalyst. Therefore, the absorption property of samples was investigated by the UV-Vis diffuse reflectance spectroscopy and the results are shown in Figure 5.

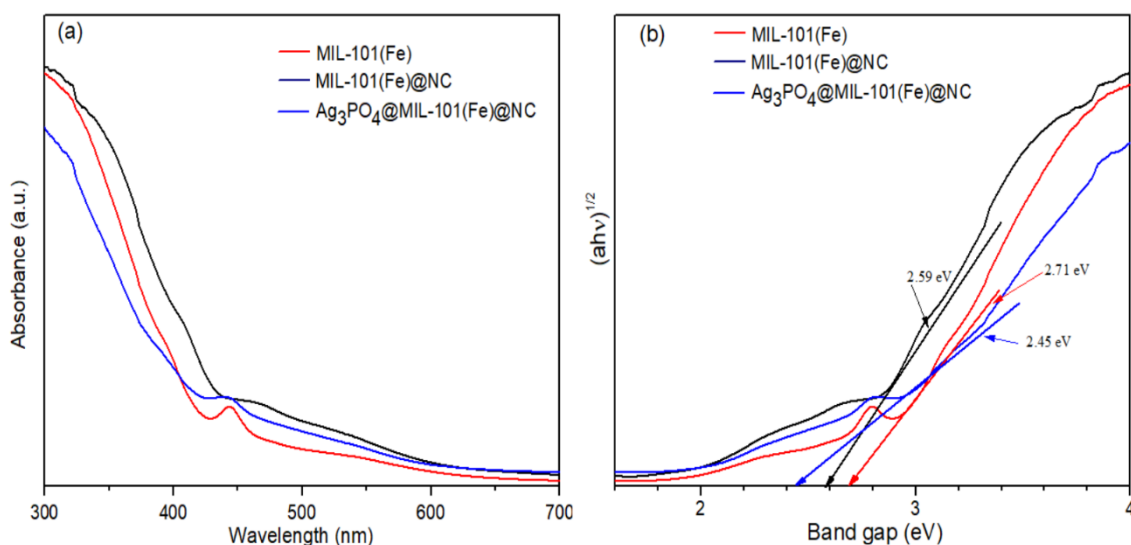


Figure 5 : a) UV-vis DRS of MIL-101(Fe), MIL-101(Fe)@NC and Ag_3PO_4 @MIL-101(Fe)@NC composites; b) Band gap estimation of MIL-101(Fe), MIL-101(Fe)@NC and Ag_3PO_4 @MIL-101(Fe)@NC composites

As can be observed from Figure 5a, the absorption response of MIL-101(Fe) in the visible region might be related to the optical transition of ligand-to metal charge transfer or a direct excitation of the Fe-O clusters by visible light irradiation [42]. MIL-101(Fe) had the ability to absorb light at about 457 nm compared to MIL-101(Fe)@NC and Ag_3PO_4 @MIL-101(Fe)@NC composites which had the ability to absorb light at 478 nm and 506 nm, respectively.

The bandgap energies of the samples could be estimated by Tauc's plots:

$$\alpha h\nu = A(h\nu - E_g)^{n/2} \quad (3)$$

where α , h , ν , A , and E_g are indicative of the absorption coefficient, Planck's constant, light frequency, constant value, and bandgap energy, and n is 1 to 4 for direct and indirect bandgap semiconductor, respectively. The plot of $(\alpha h\nu)^{1/2}$ versus

$h\nu$ is exhibited for MIL-101(Fe) and the composite. Herein, the optical band gaps of MIL-101(Fe), MIL-101(Fe)@NC, Ag_3PO_4 @MIL-101(Fe)@NC composite approximately 2.71, 2.59, 2.45 eV respectively.

The strong absorption in the visible light regions of MIL-101(Fe)@NC composite implies that the electrostatic interaction between MIL-101(Fe) and nanocellulose increased the material stability and improved absorption in visible light. Additionally, Ag_3PO_4 is a photocatalyst with bandgap energy about 2.45 eV [12], thus, photogenerated holes in Ag_3PO_4 particles fastly transfer to MIL-101(Fe), whereas photon-generated electrons migrate to the surface of Ag_3PO_4 . In such a way, the photoinduced electron-hole pairs can be effectively separated, prevents the charge recombination, leading to the higher photocatalytic activity of composite.

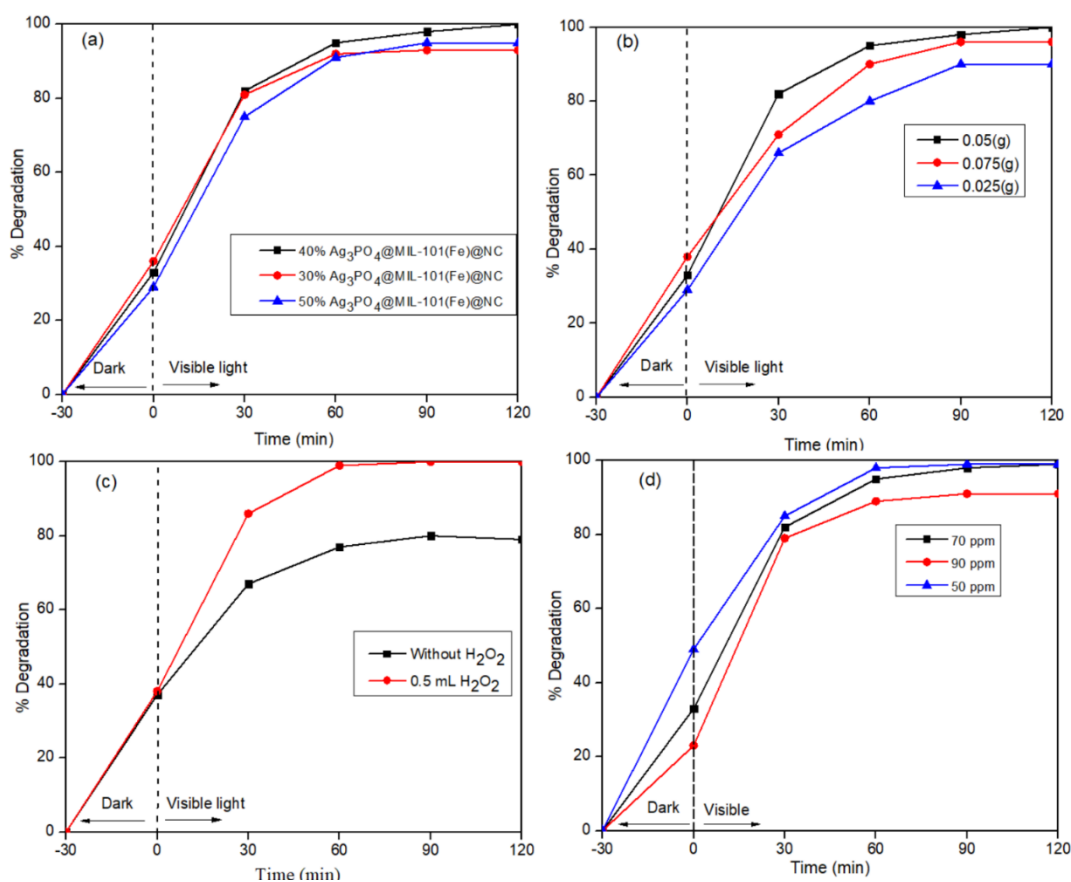
Photocatalytic activity test

Figure 6: Photodegradation of RR 195 under various reaction conditions of (a) mass contents of Ag_3PO_4 , (b) photocatalyst dosage, (c) effect of oxidation agent (H_2O_2), (d) concentration of the TC
Reaction conditions: Xe Lamp light (125 W), environment temperature (30 °C), pH = 6.5

Effect of Ag_3PO_4 contents

The improvement in photocatalytic efficiency was exhibited by the composite Ag_3PO_4 @MIL-101(Fe)@NC, as a result of the synergetic effects between the photocatalytic active phase (Ag_3PO_4) and the MIL-101(Fe)@NC support that increased sunlight absorption and efficiently separated the electron-hole pairs. Fig.6a shows that the mass content of Ag_3PO_4 has affected the photocatalytic activities of composite. The pure Ag_3PO_4 displays a low photocatalytic efficiency in TC degradation, and 68% TC was degraded in 120 min under visible light irradiation. This indicates that there is a recombination of photoinduced electron and holes pairs, thus significantly decreasing the photocatalytic efficiency in the TC degradation. The 40% Ag_3PO_4 @MIL-101(Fe)@NC exhibited the highest photocatalytic performance, degrading 99.9% after 120 min of irradiation. In contrast, with 50% Ag_3PO_4 @MIL-101(Fe)@NC, the photodegradation efficiency

decreased from 99.9% to 95.4% after 120 min of irradiation. These results could be explained that in the photocatalytic process, Ag° nanoparticles are produced by the partial reduction between Ag_3PO_4 and photogenerated electrons. The Ag metal plays a role of traps in the photogenerated electrons and thus inhibits the further decomposition of Ag_3PO_4 [43]. Therefore, the formed Ag° nanoparticles can effectively promote charge separation and enhance the photocatalytic activity of 40% Ag_3PO_4 @MIL-101(Fe)@NC. Besides, the use of the MIL-101(Fe)@NC composite prevents the recombination of the photogenerated electron-hole pairs and increased the adsorption ability of the material. However, increasing the mass content of Ag_3PO_4 to 50% can lead to an excess of the active phase that prevents the transfer of electrons and holes in this catalyst.

Effect of photocatalyst dosage

The photocatalyst dosage is also an important parameter for optimizing the reactional conditions. Therefore, the effect of photocatalyst dosage on the degradation of TC was investigated with dosage from 25 mg to 75 mg, and the result shown was in Fig.6b. It was observed that degradation efficiency increased from 90.6% to 99.7% when catalyst dosage increased from 25 mg to 50 mg, which decreased thereafter. The enhanced photodegradation efficiency could be attributed to increasing the number of active sites on the $\text{Ag}_3\text{PO}_4@\text{MIL-101}(\text{Fe})@\text{NC}$ surface as a result of the increased catalyst dosage [44]. However, if the catalyst dosage is further increased, the suspended particles of the $\text{Ag}_3\text{PO}_4@\text{MIL-101}(\text{Fe})@\text{NC}$ aggregate together and lead to reduce the amount of visible light transferring the active sites of the catalyst and consequently, the number of e^-/h^+ pairs as well as photocatalytic efficiency decreases [45].

Effect of H_2O_2 oxidizing agent

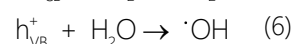
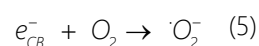
H_2O_2 acted as the source of oxidation because it consumes conduction band electrons to form active valence band holes that oxidize TC. The reaction between conduction band electrons formed free radical anions ($\cdot\text{O}_2^-$ and $\cdot\text{OH}$). As shown in Fig.6 (c), after 120 min, about 80% of TC was degraded without using H_2O_2 . However, about 99% TC was degraded by the presence of the 0.5 mL H_2O_2 . This result indicated that the assistance of H_2O_2 was needed for the degradation of TC over the 40% $\text{Ag}_3\text{PO}_4@\text{MIL-101}(\text{Fe})@\text{NC}$.

Effect of TC concentration

Photocatalytic degradation of TC over 40% $\text{Ag}_3\text{PO}_4@\text{MIL-101}(\text{Fe})@\text{CN}$ catalyst was studied by varying the initial TC concentration at constant photocatalyst dosage (50 mg). It can be seen in Fig. 6d that as the initial TC concentration increased from 50 ppm to 90 ppm, the photodegradation efficiency decreased from 99.9% to 90%. The presumed reason is that when the initial TC concentration increased, more TC molecules can be adsorbed on the catalyst surface. A large amount of adsorbed TC and its intermediates in the degradation process might have an inhibitive effect on the further photocatalytic degradation of TC because of the fewer free sites on the catalyst surface for receiving photons.

As discussed above, in the photocatalytic process, Ag° nanoparticles could be produced by the partial

reduction between Ag_3PO_4 and photogenerated electrons. Ag could trap the generated electrons and thus prevent the recombination of photogenerated electron-hole pairs. Furthermore, a large quantity of electron-hole pairs are generated inside Ag_3PO_4 , the electrons trapped by O_2 molecules on the catalyst surface will create $\cdot\text{O}_2^-$ and holes react with H_2O or OH^- to create $\cdot\text{OH}$. The reactions that take place in the TC photocatalytic degradation process using $\text{Ag}_3\text{PO}_4@\text{MIL-101}(\text{Fe})@\text{NC}$ photocatalyst are described as follow:



According to Longbao Yu *et al.* [46], $\cdot\text{O}_2^-$ plays a major role in the TC decomposition and intermediate products in the TC decomposition can be described as follows: firstly, the TC molecular ($m/z=445$) was oxidized to form the compound ($\text{C}_{22}\text{H}_{23}\text{N}_2\text{O}_7$, $m/z=427$), subsequently, $\text{C}_{22}\text{H}_{20}\text{NO}_7$ ($m/z=410$) had been formed through the deamination reaction and esterification process, after that, this compound was oxidized to the ester bond and the C=C bond to form a compound with $m/z=398$ ($\text{C}_{21}\text{H}_{20}\text{NO}_7$), and then, the cyclotriene structure was oxidized to open the ring and formed the molecular with $m/z=315$ ($\text{C}_{18}\text{H}_{19}\text{O}_5$), finally, the further oxidation reaction formed the smaller molecules such as $\text{C}_{17}\text{H}_{19}\text{O}_4$ ($m/z=287$) and $\text{C}_8\text{H}_9\text{O}_2$ ($m/z=137$).

Conclusions

In summary, we have demonstrated that the $\text{Ag}_3\text{PO}_4@\text{MIL-101}(\text{Fe})@\text{nanocellulose}$ composite is an effective visible light photocatalyst. The presence of $\text{MIL-101}(\text{Fe})@\text{nanocellulose}$ support reduced the bandgap energy, prevents recombination of the photogenerated electron-hole pairs, which significantly improves the photocatalytic efficiency. $\text{Ag}_3\text{PO}_4@\text{MIL-101}(\text{Fe})@\text{nanocellulose}$ has a narrow bandgap energy of approximately 2.45 eV, Tetracycline degradation efficiency reached 99.7% after 120 min under visible light irradiation. The use of bagasse to synthesis cellulose and recycled PET will help to reduce environmental pollution and protect the environment from further pollution.

Acknowledgements

The work is supported by the Ministry of Education and Training of Vietnam (No. B2021-MDA-03).

References

1. C. G. Daughton and T. A. Ternes, Pharmaceuticals and personal care products in the environment: agents of subtle change?, *Environ. Health Perspect.*, vol. 107, no. suppl 6 (1999) 907–938. <https://doi.org/10.1289/ehp.99107s6907>
2. I. Dalmázio, M. O. Almeida, R. Augusti, and T. M. A. Alves, Monitoring the degradation of tetracycline by ozone in aqueous medium via atmospheric pressure ionization mass spectrometry, *J. Am. Soc. Mass Spectrom.*, vol. 18, no. 4, (2007) 679–687. <https://doi.org/10.1016/j.jasms.2006.12.001>
3. I. R. Bautitz and R. F. P. Nogueira, Degradation of tetracycline by photo-Fenton process—Solar irradiation and matrix effects, *J. Photochem. Photobiol. A Chem.*, vol. 187, no. 1 (2007) 33–39. <https://doi.org/10.1016/j.jphotochem.2006.09.009>
4. H. Sanderson et al., Dissipation of oxytetracycline, chlortetracycline, tetracycline and doxycycline using HPLC–UV and LC/MS/MS under aquatic semi-field microcosm conditions, *Chemosphere*, vol. 60, no. 5, (2005) 619–629. <https://doi.org/10.1016/j.chemosphere.2005.01.035>
5. J. W. Fritz and Y. Zuo, Simultaneous determination of tetracycline, oxytetracycline, and 4-epitetracycline in milk by high-performance liquid chromatography, *Food Chem.*, vol. 105, no. 3 (2007) 1297–1301. <https://doi.org/10.1016/j.foodchem.2007.03.047>
6. A. K. Sarmah, M. T. Meyer, and A. B. A. Boxall, A global perspective on the use, sales, exposure pathways, occurrence, fate and effects of veterinary antibiotics (VAs) in the environment, *Chemosphere*, vol. 65, no. 5 (2006) 725–759. <https://doi.org/10.1016/j.chemosphere.2006.03.026>
7. X.-D. Zhu, Y.-J. Wang, R.-J. Sun, and D.-M. Zhou, Photocatalytic degradation of tetracycline in aqueous solution by nanosized TiO₂, *Chemosphere*, vol. 92, no. 8 (2013) 925–932. <http://dx.doi.org/10.1016/j.chemosphere.2013.02.066>
8. C. Reyes et al., Degradation and inactivation of tetracycline by TiO₂ photocatalysis, *J. Photochem. Photobiol. A Chem.*, vol. 184, no. 1–2 (2006) 141–146. <http://dx.doi.org/10.1016/j.chemosphere.2013.02.066>
9. R. A. Palominos, M. A. Mondaca, A. Giraldo, G. Peñuela, M. Pérez-Moya, and H. D. Mansilla, Photocatalytic oxidation of the antibiotic tetracycline on TiO₂ and ZnO suspensions, *Catal. Today*, vol. 144, no. 1–2 (2009) 100–105. <https://doi.org/10.1016/j.cattod.2008.12.031>
10. Z. Yi et al., An orthophosphate semiconductor with photooxidation properties under visible-light irradiation, *Nat. Mater.*, (2010) <https://doi.org/10.1038/nmat2780>
11. H. Zhai et al., Effect of chemical etching by ammonia solution on the microstructure and photocatalytic activity of Ag₃PO₄ photocatalyst, *Appl. Catal. A Gen.*, vol. 528 (2016) 104–112. <http://dx.doi.org/10.1016/j.apcata.2016.10.003>
12. M. Al Kausor, S. Sen Gupta, and D. Chakraborty, Ag₃PO₄-based nanocomposites and their applications in photodegradation of toxic organic dye contaminated wastewater: Review on material design to performance enhancement, *Journal of Saudi Chemical Society.*, vol. 24, (2020) 20–24. <https://doi.org/10.1016/j.jscs.2019.09.001>
13. D. J. Martin et al., Efficient visible driven photocatalyst, silver phosphate: performance, understanding and perspective, *Chem. Soc. Rev.*, vol. 44, no. 21 (2015) 7808–7828. <https://doi.org/10.1039/C5CS00380F>
14. W. da S. Pereira et al., Influence of Cu substitution on the structural ordering, photocatalytic activity and photoluminescence emission of Ag_{3-2x}Cu_xPO₄ powders, *Appl. Surf. Sci.*, vol. 440 (2018) 61–72. <http://dx.doi.org/10.1016/j.apsusc.2017.12.202>
15. F.-R. Wang, J.-D. Wang, H.-P. Sun, J.-K. Liu, and X.-H. Yang, Plasmon-enhanced instantaneous photocatalytic activity of Au@ Ag₃PO₄ heterostructure targeted at emergency treatment of environmental pollution, *J. Mater. Sci.*, vol. 52, no. 5 (2017) 2495–2510. <https://link.springer.com/article/10.1007%2Fs10853-016-0544-x>
16. X. Xie et al., Tuning the bandgap of photo-sensitive polydopamine/Ag₃PO₄/graphene oxide coating for rapid, noninvasive disinfection of implants, *ACS Cent. Sci.*, vol. 4, no. 6 (2018) 724–738. <http://dx.doi.org/10.1021/acscentsci.8b00177>
17. Q. Yang, Q. Xu, and H.-L. Jiang, Metal–organic frameworks meet metal nanoparticles: synergistic effect for enhanced catalysis, *Chem. Soc. Rev.*, vol. <https://doi.org/10.51316/jca.2021.079>

- 46, no. 15 (2017) 4774–4808.
<https://doi.org/10.1039/C6CS00724D>
18. L. Chen, R. Luque, and Y. Li, Controllable design of tunable nanostructures inside metal–organic frameworks, *Chem. Soc. Rev.*, vol. 46, no. 15 (2017) 4614–4630.
<https://doi.org/10.1039/C6CS00537C>
 19. G. Wyszogrodzka, B. Marszałek, B. Gil, and P. Dorożyński, Metal-organic frameworks: mechanisms of antibacterial action and potential applications, *Drug Discov. Today*, vol. 21, no. 6 (2016) 1009–1018.
<https://doi.org/10.1016/j.drudis.2016.04.009>
 20. J. Li, L. Wang, Y. Liu, P. Zeng, Y. Wang, and Y. Zhang, Removal of Berberine from Wastewater by MIL-101 (Fe): Performance and Mechanism, *ACS omega*, vol. 5, no. 43 (2020) 27962–27971.
<https://doi.org/10.1021/acsomega.0c03422>
 21. T. M. Budnyak, A. Slabon, and M. H. Sipponen, Lignin–inorganic interfaces: chemistry and applications from adsorbents to catalysts and energy storage materials, *ChemSusChem*, vol. 13, no. 17 (2020) 4344.
<https://doi.org/10.1002/cssc.202000216>
 22. M. Kaushik and A. H. Moores, Nanocelluloses as versatile supports for metal nanoparticles and applications in catalysis, *Green Chem.*, vol. 18 (2016) 622–637.
<https://doi.org/10.1039/C5GC02500A>
 23. P. R. Sharma, S. K. Sharma, R. Antoine, and B. S. Hsiao, Efficient removal of arsenic using zinc oxide nanocrystal-decorated regenerated microfibrillated cellulose scaffolds, *ACS Sustain. Chem. Eng.*, vol. 7, no. 6 (2019) 6140–6151.
<https://doi.org/10.1021/acssuschemeng.8b06356>
 24. M. Rathod, P. G. Moradeeya, S. Haldar, and S. Basha, Nanocellulose/TiO₂ composites: preparation, characterization and application in the photocatalytic degradation of a potential endocrine disruptor, mefenamic acid, in aqueous media, *Photochem. Photobiol. Sci.*, vol. 17, no. 10 (2018) 1301–1309.
<https://doi.org/10.1039/C8PP00156A>
 25. H.-Y. Yu, G.-Y. Chen, Y.-B. Wang, and J.-M. Yao, A facile one-pot route for preparing cellulose nanocrystal/zinc oxide nanohybrids with high antibacterial and photocatalytic activity, *Cellulose*, vol. 22, no. 1 (2015) 261–273.
<http://dx.doi.org/10.1007/s10570-014-0491-0>
 26. R. J. Moon, A. Martini, J. Nairn, J. Simonsen, and J. Youngblood, Cellulose nanomaterials review: structure, properties and nanocomposites, *Chem. Soc. Rev.*, vol. 40, no. 7 (2011) 3941–3994.
<https://doi.org/10.1039/C0CS00108B>
 27. H. V. Doan et al., Improved photodegradation of anionic dyes using a complex graphitic carbon nitride and iron-based metal-organic framework material, *Faraday Discuss* (2021).
<https://doi.org/10.1039/D1FD00010A>
 28. N. Pa'e, W. C. Liew, and I. I. Muhamad, Production of cellulose nano-crystals from bacterial fermentation, *Mater. Today Proc.*, vol. 7 (2019) 754–762.
<https://doi.org/10.1016/j.matpr.2018.12.071>
 29. K. Huang et al., One-step synthesis of Ag₃PO₄/Ag photocatalyst with visible-light photocatalytic activity, *Mater. Res.*, vol. 18 (2015) 939–945.
<http://dx.doi.org/10.1590/1516-1439.346614>
 30. B. M. Cherian et al., Cellulose nanocomposites with nanofibres isolated from pineapple leaf fibers for medical applications, *Carbohydr. Polym.*, vol. 86, no. 4 (2011) 1790–1798.
<https://doi.org/10.1016/j.carbpol.2011.07.009>
 31. J. I. Morán, V. A. Alvarez, V. P. Cyras, and A. Vázquez, Extraction of cellulose and preparation of nanocellulose from sisal fibers, *Cellulose*, vol. 15, no. 1 (2008) 149–159.
<http://dx.doi.org/10.1007/s10570-007-9145-9>
 32. E. Abraham et al., Extraction of nanocellulose fibrils from lignocellulosic fibres: A novel approach, *Carbohydr. Polym.*, vol. 86, no. 4, (2011) 1468–1475.
<https://doi.org/10.1016/j.carbpol.2011.06.034>
 33. M. Kandiah, S. Usseglio, S. Svelle, U. Olsbye, K. P. Lillerud, and M. Tilset, Post-synthetic modification of the metal–organic framework compound UiO-66, *J. Mater. Chem.*, vol. 20, no. 44, (2010) 9848–9851.
<https://doi.org/10.1039/C0JM02416C>
 34. T. Guo, K. Wang, G. Zhang, and X. Wu, A novel α -Fe₂O₃@g-C₃N₄ catalyst: synthesis derived from Fe-based MOF and its superior photo-Fenton performance, *Appl. Surf. Sci.*, vol. 469, (2019) 331–339.
<https://doi.org/10.1016/j.apsusc.2018.10.183>
 35. Q. Wu, P. Wang, F. Niu, C. Huang, Y. Li, and W. Yao, A novel molecular sieve supporting material for enhancing activity and stability of Ag₃PO₄ photocatalyst, *Appl. Surf. Sci.*, vol. 378 (2016) 552–563.
<http://dx.doi.org/10.1016/j.apsusc.2016.03.158>

36. S. Lin, L. Liu, Y. Liang, W. Cui, and Z. Zhang, Oil-in-water self-assembled synthesis of Ag@ AgCl nanoparticles on flower-like Bi₂O₂CO₃ with enhanced visible-light-driven photocatalytic activity, *Materials (Basel)*, vol. 9, no. 6, (2016) 486. <https://doi.org/10.3390/ma9060486>
37. X. Q. Tang, Y. D. Zhang, Z. W. Jiang, D. M. Wang, C. Z. Huang, and Y. F. Li, Fe₃O₄ and metal–organic framework MIL-101 (Fe) composites catalyze luminol chemiluminescence for sensitively sensing hydrogen peroxide and glucose, *Talanta*, vol. 179, (2018) 43–50. <https://doi.org/10.1016/j.talanta.2017.10.049>
38. L. He, Y. Dong, Y. Zheng, Q. Jia, S. Shan, and Y. Zhang, A novel magnetic MIL-101 (Fe)/TiO₂ composite for photo degradation of tetracycline under solar light, *J. Hazard. Mater.*, vol. 361 (2019) 85–94. <http://dx.doi.org/10.1016/j.jhazmat.2018.08.079>
39. X. Zhao, G. Zhang, and Z. Zhang, TiO₂-based catalysts for photocatalytic reduction of aqueous oxyanions: State-of-the-art and future prospects, *Environ. Int.*, vol. 136, (2020) 105453. <https://doi.org/10.1016/j.envint.2019.105453>
40. T. M. P. Nguyen et al., Phosphate adsorption by silver nanoparticles-loaded activated carbon derived from tea residue, *Sci. Rep.*, vol. 10, no. 1 (2020) 1–13. <https://www.nature.com/articles/s41598-020-60542-0>
41. Q. Gui, B. Fu, Y. He, S. Lyu, Y. Ma, and Y. Wang, Visualizing thermal distribution through hydrogel confined ionic system, *Iscience*, vol. 24, no. 2 (2021) 102085. <http://dx.doi.org/10.1016/j.isci.2021.102085>
42. L. Wang et al., Altered brain activities associated with craving and cue reactivity in people with Internet gaming disorder: Evidence from the comparison with recreational Internet game users, *Front. Psychol.*, vol. 8 (2017) 1150. <https://doi.org/10.3389/fpsyg.2017.01150>
43. J.-W. Xu, Z.-D. Gao, K. Han, Y. Liu, and Y.-Y. Song, Synthesis of magnetically separable Ag₃PO₄/TiO₂/Fe₃O₄ heterostructure with enhanced photocatalytic performance under visible light for photoinactivation of bacteria, *ACS Appl. Mater. Interfaces*, vol. 6, no. 17 (2014) 15122–15131. <https://doi.org/10.1021/am5032727>
44. J. Inamdar and S. K. Singh, Photocatalytic detoxification method for zero effluent discharge in dairy industry: Effect of operational parameters, *Int. J. Chem. Biol. Eng.*, vol. 1, no. 4 (2008) 160–164. <https://doi.org/10.5281/zenodo.1076514>
45. S. Ahmed, M. G. Rasul, W. N. Martens, R. Brown, and M. A. Hashib, Heterogeneous photocatalytic degradation of phenols in wastewater: A review on current status and developments, *Desalination*. 2010. <https://doi.org/10.1016/j.desal.2010.04.062>
46. L. Yu, Z. Ye, J. Li, C. Ma, X. Liu, H. Wang, L. Tang, P. Huo and Y. Yan, Photocatalytic Degradation Mechanism of Tetracycline by Ag@ ZnO/C Core–Shell Plasmonic Photocatalyst Under Visible Light,” *Nano*, vol. 13, no. 06 (2018) 1850065. <https://doi.org/10.1142/S1793292018500650>